

Title: Polarized X-rays Constrain The Disk-Jet Geometry in a Black Hole X-ray Binary

Henric Krawczynski¹, Fabio Muleri², Michal Dovčiak³, Alexandra Veledina^{4,5,6}, Nicole Rodriguez Caverio¹, Jiri Svoboda³, Adam Ingram⁷, Giorgio Matt⁸, Javier A. Garcia⁹, Vladislav Loktev⁴, Michela Negro^{10,11,12}, Juri Poutanen^{4,6}, Takao Kitaguchi¹³, Jakub Podgorný^{14,3,15}, John Rankin², Wenda Zhang¹⁶, Andrei Berdyugin⁴, Svetlana V. Berdyugina¹⁷, Stefano Bianchi⁸, Dmitry Blinov^{18,19}, Fiamma Capitanio², Niccolò Di Lalla²⁰, Paul Draghis²¹, Sergio Fabiani², Masato Kagitani²², Vadim Kravtsov⁴, Sebastian Kiehlmann^{18,19}, Luca Latronico²³, Alexander A. Lutovinov⁶, Nikos Mandarakas^{18,19}, Frédéric Marin¹⁴, Andrea Marinucci²⁴, Jon Miller²¹, Tsunefumi Mizuno²⁵, Sergey V. Molkov⁶, Nicola Omodei²⁰, Pierre-Olivier Petrucci²⁶, Ajay Ratheesh², Takeshi Sakanoi²², Andrei N. Semena⁶, Raphael Skalidis^{18,19}, Paolo Soffitta², Allyn F. Tennant²⁷, Phillipp Thalhammer²⁸, Francesco Tombesi^{29,30,31}, Martin C. Weisskopf²⁷, Joern Wilms²⁸, Sixuan Zhang²⁵, Iván Agudo³², Lucio A. Antonelli^{33,34}, Matteo Bachetti³⁵, Luca Baldini^{36,37}, Wayne H. Baumgartner²⁷, Ronaldo Bellazzini³⁶, Stephen D. Bongiorno²⁷, Raffaella Bonino^{23,38}, Alessandro Brez³⁶, Niccolò Bucciantini^{39,40,41}, Simone Castellano³⁶, Elisabetta Cavazzuti²⁴, Stefano Ciprini^{30,34}, Enrico Costa², Alessandra De Rosa², Ettore Del Monte², Laura Di Gesu²⁴, Alessandro Di Marco², Immacolata Donnarumma²⁴, Victor Doroshenko^{42,6}, Steven R. Ehlert²⁷, Teruaki Enoto¹³, Yuri Evangelista², Riccardo Ferrazzoli², Shuichi Gunji⁴³, Kiyoshi Hayashida⁴⁴, Jeremy Heyl⁴⁵, Wataru Iwakiri⁴⁶, Svetlana G. Jorstad^{47,48}, Vladimir Karas³, Jeffery J. Kolodziejczak²⁷, Fabio La Monaca², Ioannis Liodakis⁴⁹, Simone Maldera²³, Alberto Manfreda³⁶, Alan P. Marscher⁴⁷, Herman L. Marshall⁵⁰, Francesco Massaro^{23,38}, Ikuyuki Mitsuishi⁵¹, C.-Y. Ng⁵², Stephen L. O'Dell²⁷, Chiara Oppedisano²³, Alessandro Papitto³³, George G. Pavlov⁵³, Abel L. Peirson²⁰,

Matteo Perri^{34,33}, Melissa Pesce-Rollins³⁶, Maura Pilia³⁵, Andrea Possenti³⁵,
Simonetta Puccetti³⁴, Brian D. Ramsey²⁷, Roger W. Romani²⁰, Carmelo
Sgrò³⁶, Patrick Slane⁵⁴, Gloria Spandre³⁶, Toru Tamagawa¹³, Fabrizio
Tavecchio⁵⁵, Roberto Taverna⁵⁶, Yuzuru Tawara⁵¹, Nicolas E. Thomas²⁷,
Alessio Trois³⁵, Sergey Tsygankov^{4,6}, Roberto Turolla^{56,57}, Jacco Vink⁵⁸,
Kinwah Wu⁵⁷, Fei Xie⁵⁹, and Silvia Zane⁵⁷

¹Physics Department and McDonnell Center for the Space Sciences,
Washington University in St. Louis, St. Louis, MO 63130, USA

²INAF Istituto di Astrofisica e Planetologia Spaziali, Via del Fosso del
Cavaliere 100, 00133 Roma, Italy

³Astronomical Institute of the Czech Academy of Sciences, Boční II 1401/1,
14100 Praha 4, Czech Republic

⁴Department of Physics and Astronomy, 20014 University of Turku, Finland

⁵Nordita, KTH Royal Institute of Technology and Stockholm University,
Roslagstullsbacken 23, SE-10691 Stockholm, Sweden

⁶Space Research Institute of the Russian Academy of Sciences, Profsoyuznaya
Str. 84/32, Moscow 117997, Russia

⁷School of Mathematics, Statistics, and Physics, Newcastle University,
Newcastle upon Tyne NE1 7RU, UK

⁸Dipartimento di Matematica e Fisica, Università degli Studi Roma Tre, Via
della Vasca Navale 84, 00146 Roma, Italy

⁹California Institute of Technology, Pasadena, CA 91125, USA

¹⁰University of Maryland, Baltimore County, Baltimore, MD 21250, USA

¹¹NASA Goddard Space Flight Center, Greenbelt, MD 20771, USA

¹²Center for Research and Exploration in Space Science and Technology,
NASA/GSFC, Greenbelt, MD 20771, USA

¹³RIKEN Cluster for Pioneering Research, 2-1 Hirosawa, Wako, Saitama
351-0198, Japan

¹⁴Université de Strasbourg, CNRS, Observatoire Astronomique de Strasbourg,
UMR 7550, 67000 Strasbourg, France

¹⁵Astronomical Institute, Charles University, V Holešovičkách 2, CZ-18000
Prague, Czech Republic

- ¹⁶National Astronomical Observatories, Chinese Academy of Sciences, 20A
Datun Road, Beijing 100101, China
- ¹⁷Leibniz-Institut für Sonnenphysik, D-79104 Freiburg, Germany
- ¹⁸Institute of Astrophysics, Foundation for Research and Technology-Hellas,
GR-71110 Heraklion, Greece
- ¹⁹Department of Physics, Univ. of Crete, GR-70013 Heraklion, Greece
- ²⁰Department of Physics and Kavli Institute for Particle Astrophysics and
Cosmology, Stanford University, Stanford, California 94305, USA
- ²¹Department of Astronomy, University of Michigan, 1085 South University
Avenue, Ann Arbor, MI 48109-1107, USA
- ²²School of Sciences, Tohoku University, Aoba-ku, 980-8578 Sendai, Japan
- ²³Istituto Nazionale di Fisica Nucleare, Sezione di Torino, Via Pietro Giuria 1,
10125 Torino, Italy
- ²⁴ASI - Agenzia Spaziale Italiana, Via del Politecnico snc, 00133 Roma, Italy
- ²⁵Hiroshima Astrophysical Science Center, Hiroshima University, 1-3-1
Kagamiyama, Higashi-Hiroshima, Hiroshima 739-8526, Japan
- ²⁶Université Grenoble Alpes, CNRS, IPAG, 38000 Grenoble, France
- ²⁷NASA Marshall Space Flight Center, Huntsville, AL 35812, USA
- ²⁸Dr. Karl Remeis-Observatory and Erlangen Centre for Astroparticle Physics,
Universität Erlangen-Nürnberg, Sternwartstr. 7, 96049 Bamberg, Germany
- ²⁹Dipartimento di Fisica, Università degli Studi di Roma "Tor Vergata", Via
della Ricerca Scientifica 1, 00133 Roma, Italy
- ³⁰Istituto Nazionale di Fisica Nucleare, Sezione di Roma "Tor Vergata", Via
della Ricerca Scientifica 1, 00133 Roma, Italy
- ³¹Department of Astronomy, University of Maryland, College Park, Maryland
20742, USA
- ³²Instituto de Astrofísica de Andalucía—CSIC, Glorieta de la Astronomía s/n,
18008, Granada, Spain
- ³³INAF Osservatorio Astronomico di Roma, Via Frascati 33, 00078 Monte
Porzio Catone (RM), Italy
- ³⁴Space Science Data Center, Agenzia Spaziale Italiana, Via del Politecnico
snc, 00133 Roma, Italy
- ³⁵INAF Osservatorio Astronomico di Cagliari, Via della Scienza 5, 09047

Selargius (CA), Italy

³⁶Istituto Nazionale di Fisica Nucleare, Sezione di Pisa, Largo B. Pontecorvo
3, 56127 Pisa, Italy

³⁷Dipartimento di Fisica, Università di Pisa, Largo B. Pontecorvo 3, 56127
Pisa, Italy

³⁸Dipartimento di Fisica, Università degli Studi di Torino, Via Pietro Giuria 1,
10125 Torino, Italy

³⁹INAF Osservatorio Astrofisico di Arcetri, Largo Enrico Fermi 5, 50125
Firenze, Italy

⁴⁰Dipartimento di Fisica e Astronomia, Università degli Studi di Firenze, Via
Sansone 1, 50019 Sesto Fiorentino (FI), Italy

⁴¹Istituto Nazionale di Fisica Nucleare, Sezione di Firenze, Via Sansone 1,
50019 Sesto Fiorentino (FI), Italy

⁴²Institut für Astronomie und Astrophysik, Universität Tübingen, Sand 1,
72076 Tübingen, Germany

⁴³Yamagata University, 1-4-12 Kojirakawa-machi, Yamagata-shi 990-8560,
Japan

⁴⁴Osaka University, 1-1 Yamadaoka, Suita, Osaka 565-0871, Japan

⁴⁵University of British Columbia, Vancouver, BC V6T 1Z4, Canada

⁴⁶Department of Physics, Faculty of Science and Engineering, Chuo
University, 1-13-27 Kasuga, Bunkyo-ku, Tokyo 112-8551, Japan

⁴⁷Institute for Astrophysical Research, Boston University, 725 Commonwealth
Avenue, Boston, MA 02215, USA

⁴⁸Department of Astrophysics, St. Petersburg State University, Universitetsky
pr. 28, Petrodvoretz, 198504 St. Petersburg, Russia

⁴⁹Finnish Centre for Astronomy with ESO, 20014 University of Turku,
Finland

⁵⁰MIT Kavli Institute for Astrophysics and Space Research, Massachusetts
Institute of Technology, 77 Massachusetts Avenue, Cambridge, MA 02139,
USA

⁵¹Graduate School of Science, Division of Particle and Astrophysical Science,
Nagoya University, Furo-cho, Chikusa-ku, Nagoya, Aichi 464-8602, Japan

⁵²Department of Physics, The University of Hong Kong, Pokfulam, Hong

Kong

⁵³Department of Astronomy and Astrophysics, Pennsylvania State University,
University Park, PA 16802, USA

⁵⁴Center for Astrophysics, Harvard & Smithsonian, 60 Garden St, Cambridge,
MA 02138, USA

⁵⁵INAF Osservatorio Astronomico di Brera, Via E. Bianchi 46, 23807 Merate
(LC), Italy

⁵⁶Dipartimento di Fisica e Astronomia, Università degli Studi di Padova, Via
Marzolo 8, 35131 Padova, Italy

⁵⁷Mullard Space Science Laboratory, University College London, Holmbury St
Mary, Dorking, Surrey RH5 6NT, UK

⁵⁸Anton Pannekoek Institute for Astronomy & GRAPPA, University of
Amsterdam, Science Park 904, 1098 XH Amsterdam, The Netherlands

⁵⁹Guangxi Key Laboratory for Relativistic Astrophysics, School of Physical
Science and Technology, Guangxi University, Nanning 530004, China

One sentence summary: For the first time, X-ray polarization reveals the configuration of matter as it is drawn into a stellar mass black hole.

Abstract: In a black hole X-ray binary (XRB) system, gas accreted from a normal star onto a black hole glows brightly in X-rays. We report on an observation of the XRB Cygnus X-1 (Cyg X-1) by the Imaging X-ray Polarimetry Explorer (*IXPE*) yielding the first highly significant detection of X-ray polarization from an accreting black hole. The electric vector polarization angle aligns with the outflowing radio jet, supporting the hypothesis that the jet is launched from the inner X-ray emitting region. The higher than expected 2–8 keV polarization degree of $4.0 \pm 0.2\%$ implies that the accretion disk is viewed more edge-on than inferred from the orbital parameters. The spectropolarimetric data reveal that the hot X-ray emitting plasma is extended in the plane of the accretion disk rather than along the jet axis.

1 Introduction

Cyg X-1 is one of the brightest and most persistent X-ray sources in the sky. The system harbors a 21.2 ± 2.2 solar-mass black hole (BH) in a 5.6 day orbit with a $40.6_{-7.1}^{+7.7}$ solar-mass star. The high-mass X-ray binary (HMXB) is at a distance of $2.22_{-0.17}^{+0.18}$ kpc from us (1). Matter from the companion star is drawn into the BH and is heated to millions of degrees. The hot incandescent gas makes the binary system an exceptionally bright source of X-rays. X-rays are thus ideally suited to reveal how BHs accrete matter, and to constrain the curved spacetimes in their vicinity. The analysis of the thermal X-ray flux and energy spectrum and the shape of the X-ray emission lines both indicate that the BH in Cyg X-1 spins rapidly with a dimensionless spin parameter $a > 0.92$ close to the maximum possible value of 1 (2, 3). Cyg X-1 exhibits furthermore a radio jet (4), making it a microquasar, i.e., a miniature sibling of radio-loud quasars, supermassive BHs with jets.

BHs are observed in different states which are thought to correspond to different configurations of the matter plunging into the BH (5–7). In the *soft* state, the X-rays are dominated by the thermal accretion disk emission, which is likely polarized because of electron scattering, and polarization information can constrain the BH spin parameter a and the BH inclination i (angle between the spin axis and the line of sight) (8–10). In the *hard* state, the emission is produced by

Compton scattering in ‘coronal’ plasma. The plasma of the corona has a temperature of ~ 100 keV, much hotter than the ~ 0.1 keV temperature of the accretion disk photosphere. The polarization of the Comptonized emission can be used to constrain the location and properties of the corona as well as the inner accretion disk (11–14). The reflection of coronal emission off the accretion disk gives rise to an emission component that includes the iron $K\alpha$ fluorescence line at ~ 6.4 keV. The line contains information about velocity of the emitting plasma and the clock speed in the plasma’s reference frame. The reflection component is expected to be polarized as well (15, 16). X-ray polarimetry is thus a unique tool to study the geometry and orientation of the X-ray emitting plasma in the direct vicinity of the BH and provide an independent measure of the BH spin.

The theoretical expectation of the Cyg X-1 polarization degree in the 2–8 keV *IXPE* band was around $\sim 1\%$ or lower depending on the state of the source (9, 10, 12, 14). These expectations are motivated by the low inclination of the system $i = 27.1 \pm 0.8$ (1σ errors) inferred from optical observations (1). Earlier polarization observations of Cyg X-1 with the *OSO-8* polarimeter at 2.6 and 5.2 keV fell short of a firm detection (17). The *POGO+* experiment set upper limits on the 19–181 keV polarization degree of $< 8.6\%$ (90% confidence) (18). Observational evidence for polarization at > 400 keV energies has been reported (19, 20), with the responsible physical mechanism still a matter of debate (21, 22). The *IXPE* mission (23), launched on 2021 December 9, is the first dedicated X-ray polarimetry mission since *OSO-8* (1975–1978) (17) and achieves the *OSO-8* sensitivity in $1/100^{\text{th}}$ of the observation time. Combining the *IXPE* 2–8 keV observations with concurrent broadband X-ray observations of the X-ray space instruments *NICER* (24) and *NuSTAR* (25) covering together the 0.2–79 keV energy band allows us to decompose the signal into the thermal disk emission, the coronal X-ray emission, and hard X-ray emission reflected off the accretion disk. The *IXPE* results give new insights into the location and geometry of the emitting plasmas, and its relation to the radio jet.

2 Observational Results

IXPE observed Cyg X-1 between 2022 May 15 and May 21 for a total net exposure of ~ 242 ksec. The source was highly variable (see the lightcurves from different instruments

on Fig. S1), with the mean flux detected by *IXPE* of $\approx 5.2 \times 10^{-9}$ ergs cm $^{-2}$ s $^{-1}$. Combining the *IXPE* energy spectrum with simultaneous *NICER* and *NuSTAR* observations shows that the source was in the hard state with the coronal and reflected emission (power-law index $\Gamma \approx 1.6$ where the specific photon flux is $dN/dE \propto E^{-\Gamma}$) dominating in the *IXPE* band. The Supplementary Material (SM) gives the full details of the analyses presented here, including the derivation of the statistical confidence intervals.

IXPE detects the linear polarization with a $> 20\sigma$ statistical confidence. The signal exhibits an unexpectedly high 2–8 keV polarization degree of $4.0 \pm 0.2\%$ at an electric vector polarization angle (PA) of $-20^\circ.7 \pm 1^\circ.4$ east of north (all error bars are 1σ). Figure 1 shows the polarization results in four energy bands. The polarization degree seems to increase with energy from $3.5 \pm 0.3\%$ at 2–3 keV to $5.8 \pm 0.8\%$ at 6–8 keV at a statistical confidence of 68.3% (SM, Table S2).

The X-ray polarization is determined by the properties of the inner accretion flow. For the rapidly spinning 21.2 solar mass BH Cyg X-1, most of the X-ray emission comes from a ~ 600 km diameter region surrounding the BH with an event horizon of a diameter of ~ 60 km. This region subtends an angle in the sky of $\sim 2 \times 10^{-9}$ arcseconds, too small to be imaged with even the best telescopes at any wavelength available today or in the foreseeable future. The orientation of the inner accretion flow can be compared to that of the radio jet imaged on much larger, billion-km spatial scales. Figure 2 shows that the X-ray polarization is parallel to the jet. The polarization degree and angle are consistent with the results of the 2.6 keV *OSO-8* observations, even though the approximate agreement of the polarization angle has to be regarded as coincidental given the low 1.8σ significance of the *OSO-8* polarization signal (26).

We fitted the *IXPE*, *NICER*, and *NuSTAR* energy spectra with a composite model including a multi-temperature black body component (thermal emission from the accretion disk), a power-law component (from multiple Compton scattering events in the corona), emission reflected off the accretion disk, and emission from more distant stationary plasma (see SM, Fig. S5 for details). For each of the emission components we allow for a constant (in energy and time) polarization degree and angle. The results indicate that the coronal emission strongly dominates the overall emission in the *IXPE* energy band, contributing $\sim 90\%$ of the observed flux. The accretion disk, and reflected emission components contribute $< 1\%$ and $\sim 10\%$ of the emission,

respectively. The results indicate that *IXPE* largely measures the polarization of the coronal emission.

We accompanied the *IXPE* observations with optical polarization observations with the DIPol-2 polarimeter mounted on the Tohoku 60 cm telescope at the Haleakala Observatory and the RoboPol polarimeter at the 1.3 m telescope of the Skinakas observatory, Greece (see SM). We measured the polarization degrees and angles in the three optical bands *B* and *V* (DIPoL-2) and *R* (DIPoL-2 and RoboPol) for different choices of nearby field stars used for the determination of the interstellar polarization. We find intrinsic optical polarization degrees between 0.8% and 1% and intrinsic optical polarization angles between -37° and -11° . The statistical and systematic errors on the polarization degree and angle are about 0.1%, and $< \sim 15^\circ$, respectively. The detailed analysis methods and results are reported in the SM (Figs. **S8-S9**, and Table **S4**). The optical polarization directions is believed to give the orientation of the orbital axis onto the sky (27).

Discussion

The *IXPE* observations reveal that the X-rays are highly polarized parallel to the radio jet. We do not find evidence for an orbital phase dependence of the polarization properties which excludes the possibility that the observed polarization originates from the scattering of X-ray photons off the companion star or its wind. We find, furthermore, that the polarization degrees and angles do not depend on the source flux (SM, Fig. **S4**). This finding indicates that the inner accretion flow emitting the bulk of the observed X-rays, rather than a distant emission component that does not vary in concert with the bulk of the emission, generates the observed 2-8 keV polarization, since the superposition of emission components with different time evolutions and polarization properties would give rise to a variable net polarization.

For symmetry reasons, any model of X-ray polarization from the inner accretion flow predicts a polarization angle predominantly parallel or perpendicular to the accretion flow. As a jet cannot be launched parallel to the accretion disk plane, the observed alignment between images of the radio jet and the X-ray polarization angle indicates that the projections on the sky of the inner accretion disk spin axis and the jet are roughly aligned. This finding validates the long-

standing hypothesis that the jets of microquasars (and, by extension, of quasars) are launched perpendicular to the inner accretion flow (at least on the plane of the sky). The approximate alignment with the optical polarization angle furthermore indicates alignment on the plane of the sky also with the binary orbital axis.

Assuming that the detected X-ray polarization stems from the Comptonization of photons in a hot plasma in the inner accretion flow, we can use the polarization results to constrain the geometry of the hot plasma, and the angle at which the observer views the plasma. The shape and location of the hot plasma, or corona, are so far poorly constrained through observations and theory (7, 28). The main result of the *IXPE* observations is that the combination of high polarization degree and polarization direction parallel to the jet imply that the coronal plasma is laterally extended in the plane of the accretion disk (see SM, Figs. **S6-S7**, and the accompanying discussion). In such models, the X-ray polarization is parallel to the spin axis of the inner disk. Such corona plasma configuration can be realized by coronal plasma sandwiching the accretion disk (e.g., as predicted by numerical accretion disk simulations (29)). An alternative configuration is a composite accretion flow with an inner geometrically thick, optically thin laterally extended region of hot plasma replacing the inner region of a geometrically thin, optically thick accretion disk, possibly owing to evaporation of the inner disk (30). If the jet is forming in the inner, magnetized region of the disk, the extraction of the disk angular momentum by the jet torque may leave a radially extended hot and optically thin corona behind (31).

The polarization data rule out models in which the corona is a narrow plasma column centered on the BH spin axis, or an extremely compact region centered on the spin axis of the BH as assumed in the idealized lamppost models commonly invoked by X-ray astronomers to interpret observations (Figs. **S6**, right panel, and the related discussion). For such models, the predicted polarization degrees tend to be smaller than the observed ones and decrease with energy in the *IXPE* band. The models that do predict polarization degrees as large as the observed ones require inclinations $i \gtrsim 85^\circ$ or coronae moving away from the black hole with velocities close to the speed of light. However, in these cases the polarization direction is perpendicular to the spin axis of the accretion disk. We disfavor these scenarios as the jet would be in the plane of the disk rather than perpendicular to it – a very unlikely configuration.

Even for the favored laterally extended coronae, the observed polarization degrees are higher

than the $\sim 1\%$ polarization degrees expected for inclinations of $\sim 27^\circ$. While coronae powered by the Comptonization of internally generated synchrotron photons can produce the observed polarization degrees for inner disk inclinations exceeding 45° , the Comptonization of disk photons requires inclinations exceeding 65° . Synchrotron seed photons are expected to have lower energies ($\sim 1\text{--}10$ eV) than accretion disk seed photons (a fraction of a keV) (32). The larger number of scatterings required to energize the former to keV energies results in higher polarization degrees. This is particularly important at the lowest *IXPE* energies, where the Comptonization of accretion disk photons tends to underpredict the observed polarization degree (Figs. S6-S7).

Our results therefore indicate that the entire system approximately aligns on the plane of the sky but that the inner disk is misaligned with the binary orbital axis in the dimension of our sight line. As the bodies of a stellar system tend to all orbit and spin around the same axis, we offer here two explanations for the mismatch between the inner accretion disk and the orbital inclinations. The supernova explosion forming the BH may have left the BH with a misaligned spin. Bardeen and Petterson conjectured that the combination of the corkscrew orbits of matter orbiting spinning BHs and the viscosity of the disk will warp the inner accretion disk into the equatorial plane of the Kerr spacetime (33). Some analyses of reflected Cyg X-1 energy spectra give high Cyg X-1 inner disk inclinations comparable to the ones inferred from our polarization measurements (3, 34, 35).

Alternatively, the higher inclination may be a consequence of superorbital precession of the inner accretion disk. Observations of Cyg X-1 performed with different X-ray, optical and radio instruments indicate the presence of a superorbital periodicity that can be explained as a precession of the accretion disk (36). Our analysis of X-ray light-curves suggests that the *IXPE* observations were performed close to the superorbital phase maximizing the inner disk inclination. A counterargument to this scenario, with a precession amplitude of $\pm 15^\circ$, is the small ($\ll 15^\circ$) opening angle of the radio jet. Additional observations at different superorbital phases can be used to validate or refute this scenario. The larger inner disk inclination found here will lower the spin value inferred from the analysis of the flux and energy spectrum of the thermal emission (1, 37).

We disfavor the possibility that optically thin synchrotron emission from the base of the jet

strongly contributes to the observed polarization signal (38). The jet is unlikely to produce more than 5% of the 2–8 keV emission (21, 39) and the toroidal magnetic field structure required by the observed polarization direction produces a polarization degree well below the theoretical maximum of 75% for synchrotron emission from a region with unidirectional magnetic field (40). The overall contribution to the 2–8 keV polarization from the jet base will therefore be well below the observed level.

The results presented in this paper demonstrate that X-ray polarization opens up a new chapter in our studies of BH accretion.

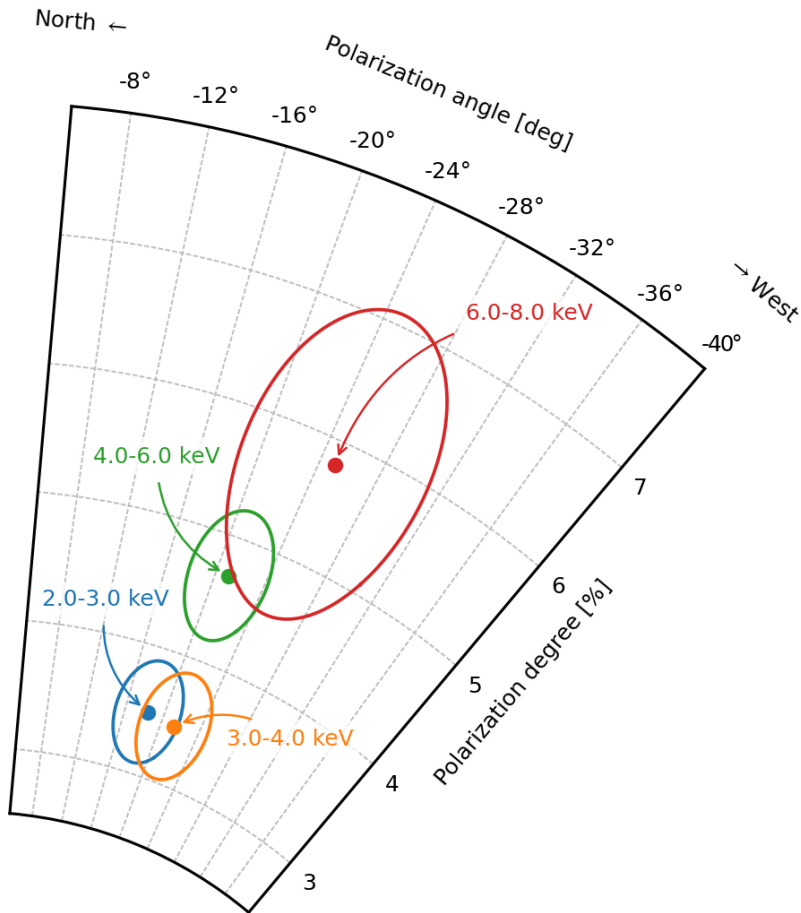


Figure 1: Energy-dependent X-ray polarization of Cyg X-1. *IXPE* detects the linear polarization of the 2–8 keV X-ray emission from the XRB Cyg X-1 with high statistical significance. The figure shows the polarization degree (PD) and polarization angle (PA) in four energy bands. The ellipses denote the statistical significance of 68.3%.

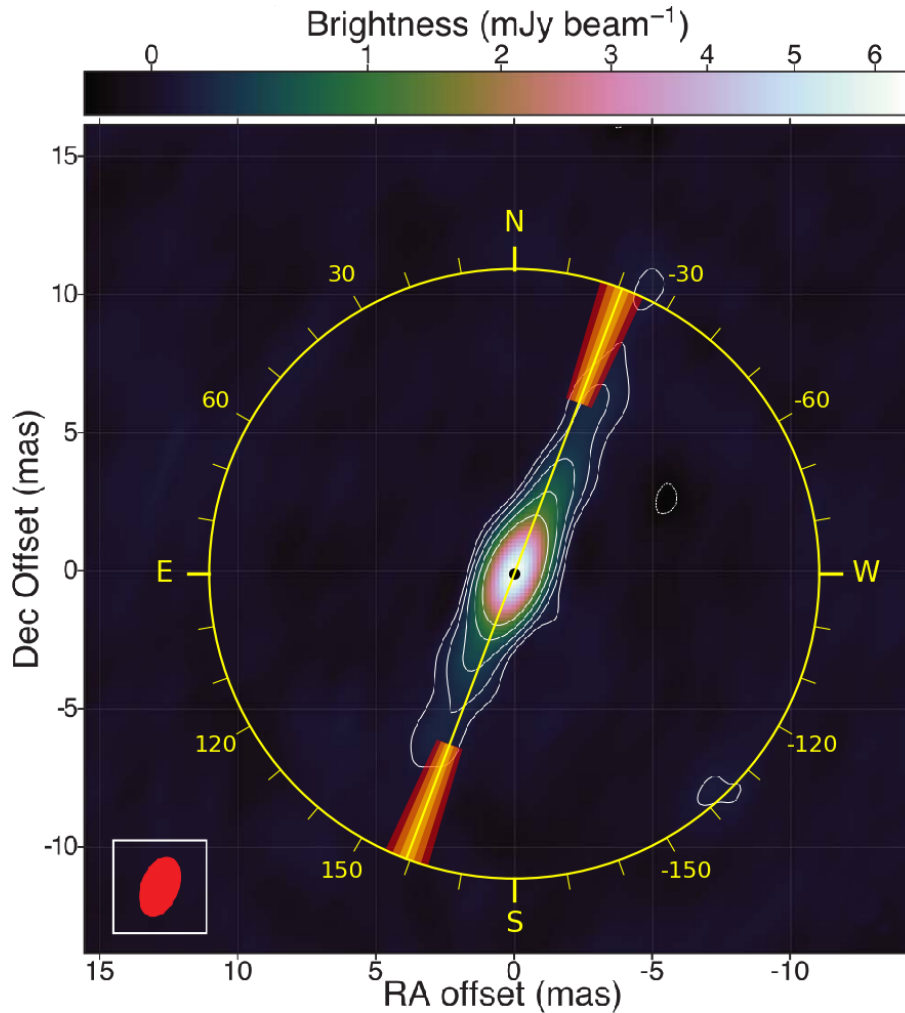


Figure 2: The X-ray polarization direction agrees well with the orientation of the radio jet imaged with the Very Large Baseline Array from (1). The 2–8 keV electric vector polarization direction is shown by the yellow line, and the one, two and three sigma confidence intervals are given by the orange to red cone segments. Note that most X-rays come from a ~ 600 km diameter region surrounding the ~ 60 km diameter BH. The 600 km large region is approximately one million times smaller than the resolution of the radio image. The width of the image corresponds to a spatial extent of 10 billion km. The coordinate offsets are in Right Ascension (RA) and Declination (Dec), J2000 equinox. The color scale shows the radio flux. The red ellipse shows the size and orientation of the synthesized radio beam.

References

1. J. C. A. Miller-Jones, *et al.*, *Science* **371**, 1046 (2021).
2. L. Gou, *et al.*, *Astrophys. J.* **790**, 29 (2014).
3. J. A. Tomsick, *et al.*, *Astrophys. J.* **855**, 3 (2018).
4. A. M. Stirling, *et al.*, *Mon. Not. R. Astron. Soc.* **327**, 1273 (2001).
5. A. A. Zdziarski, M. Gierliński, *Progr. Theor. Phys. Suppl.* **155**, 99 (2004).
6. R. A. Remillard, J. E. McClintock, *Ann. Rev. Astron. Astrophys.* **44**, 49 (2006).
7. C. Done, M. Gierliński, A. Kubota, *Astron. Astrophys. Rev.* **15**, 1 (2007).
8. P. A. Connors, T. Piran, R. F. Stark, *Astrophys. J.* **235**, 224 (1980).
9. L.-X. Li, R. Narayan, J. E. McClintock, *Astrophys. J.* **691**, 847 (2009).
10. J. D. Schnittman, J. H. Krolik, *Astrophys. J.* **701**, 1175 (2009).
11. J. Poutanen, R. Svensson, *Astrophys. J.* **470**, 249 (1996).
12. J. D. Schnittman, J. H. Krolik, *Astrophys. J.* **712**, 908 (2010).
13. W. Zhang, M. Dovčiak, M. Bursa, *Astrophys. J.* **875**, 148 (2019).
14. H. Krawczynski, B. Beheshtipour, *arXiv e-prints* p. arXiv:2201.07360 (2022).
15. G. Matt, *Mon. Not. R. Astron. Soc.* **260**, 663 (1993).
16. J. Poutanen, K. N. Nagendra, R. Svensson, *Mon. Not. R. Astron. Soc.* **283**, 892 (1996).
17. M. C. Weisskopf, *et al.*, *Astrophys. J. Lett.* **215**, L65 (1977).
18. M. Chauvin, *et al.*, *Nature Astronomy* **2**, 652 (2018).
19. P. Laurent, *et al.*, *Science* **332**, 438 (2011).

20. J. Rodriguez, *et al.*, *Astrophys. J.* **807**, 17 (2015).
21. A. A. Zdziarski, P. Pjanka, M. Sikora, Ł. Stawarz, *Mon. Not. R. Astron. Soc.* **442**, 3243 (2014).
22. F. Cangemi, *et al.*, *Astron. & Astrophys.* **650**, A93 (2021).
23. M. C. Weisskopf, *et al.*, *Journ. Astron. Telesc. Instr. Syst.* **8(2)**, 026002 (2022).
24. K. C. Gendreau, Z. Arzoumanian, T. Okajima, *Space Telescopes and Instrumentation 2012: Ultraviolet to Gamma Ray*, T. Takahashi, S. S. Murray, J.-W. A. den Herder, eds. (2012), vol. 8443 of *Society of Photo-Optical Instrumentation Engineers (SPIE) Conference Series*, p. 844313.
25. F. A. Harrison, *et al.*, *Astrophys. J.* **770**, 103 (2013).
26. K. S. Long, G. A. Chanan, R. Novick, *Astrophys. J.* **238**, 710 (1980).
27. J. C. Kemp, M. S. Barbour, T. E. Parker, L. C. Herman, *Astrophys. J. Lett.* **228**, L23 (1979).
28. C. Bambi, *et al.*, *Space Sci. Rev.* **217**, 65 (2021).
29. B. E. Kinch, J. D. Schnittman, S. C. Noble, T. R. Kallman, J. H. Krolik, *Astrophys. J.* **922**, 270 (2021).
30. F. Meyer, E. Meyer-Hofmeister, *Astron. & Astrophys.* **288**, 175 (1994).
31. P. O. Petrucci, J. Ferreira, G. Henri, J. Malzac, C. Foellmi, *Astron. & Astrophys.* **522**, A38 (2010).
32. A. Veledina, J. Poutanen, I. Vurm, *Mon. Not. R. Astron. Soc.* **430**, 3196 (2013).
33. J. M. Bardeen, J. A. Petterson, *Astrophys. J. Lett.* **195**, L65 (1975).
34. J. A. Tomsick, *et al.*, *Astrophys. J.* **780**, 78 (2014).
35. M. L. Parker, *et al.*, *Astrophys. J.* **808**, 9 (2015).

36. J. Poutanen, A. A. Zdziarski, A. Ibragimov, *Mon. Not. R. Astron. Soc.* **389**, 1427 (2008).
37. L. Gou, *et al.*, *Astrophys. J.* **742**, 85 (2011).
38. D. M. Russell, T. Shahbaz, *Mon. Not. R. Astron. Soc.* **438**, 2083 (2014).
39. D. Kantzas, *et al.*, *Mon. Not. R. Astron. Soc.* **500**, 2112 (2021).
40. M. Lyutikov, V. I. Pariev, D. C. Gabuzda, *Mon. Not. R. Astron. Soc.* **360**, 869 (2005).
41. K. A. Arnaud, *Astronomical Data Analysis Software and Systems V*, G. H. Jacoby, J. Barnes, eds. (1996), vol. 101 of *Astronomical Society of the Pacific Conference Series*, p. 17.
42. P. Freeman, S. Doe, A. Siemiginowska, *Astronomical Data Analysis*, J.-L. Starck, F. D. Murtagh, eds. (2001), vol. 4477 of *Society of Photo-Optical Instrumentation Engineers (SPIE) Conference Series*, pp. 76–87.
43. S. Doe, *et al.*, *Astronomical Data Analysis Software and Systems XVI*, R. A. Shaw, F. Hill, D. J. Bell, eds. (2007), vol. 376 of *Astronomical Society of the Pacific Conference Series*, p. 543.
44. B. L. Refsdal, *et al.*, *Proceedings of the 8th Python in Science Conference*, G. Varoquaux, S. van der Walt, J. Millman, eds. (Pasadena, CA USA, 2009), pp. 51 – 57.
45. B. Refsdal, S. Doe, D. Nguyen, A. Siemiginowska, *Proceedings of the 10th Python in Science Conference*, S. van der Walt, J. Millman, eds. (2011), pp. 10 – 16.
46. F. Kislat, B. Clark, M. Beilicke, H. Krawczynski, *Astroparticle Physics* **68**, 45 (2015).
47. L. Baldini, *et al.*, *arXiv e-prints* p. arXiv:2203.06384 (2022).
48. M. C. Weisskopf, R. F. Elsner, S. L. O’Dell, *Proc. of SPIE* (2010), vol. 7732, p. 77320E.
49. F. Muleri, *Analysis of the data from photoelectric gas polarimeters* (Springer Singapore, Eds. C. Bambi and A. Santangelo, in press).

50. T. E. Strohmayer, *Astrophys. J.* **838**, 72 (2017).
51. M. Pavlinsky, *et al.*, *Astron. & Astrophys.* **650**, A42 (2021).
52. R. Sunyaev, *et al.*, *Astron. & Astrophys.* **656**, A132 (2021).
53. M. Dovčiak, F. Muleri, R. W. Goosmann, V. Karas, G. Matt, *Astrophys. J.* **731**, 75 (2011).
54. J. Podgorný, M. Dovčiak, F. Marin, R. Goosmann, A. Róžańska, *Mon. Not. R. Astron. Soc.* **510**, 4723 (2022).
55. J. García, T. R. Kallman, R. F. Mushotzky, *Astrophys. J.* **731**, 131 (2011).
56. J. García, *et al.*, *Astrophys. J.* **768**, 146 (2013).
57. J. García, *et al.*, *Astrophys. J.* **782**, 76 (2014).
58. S. Chandrasekhar, *Radiative transfer* (Dover Publications, 1960).
59. A. M. Beloborodov, *Astrophys. J. Lett.* **510**, L123 (1999).
60. D. I. Nagirner, J. Poutanen, *Astron. & Astrophys.* **275**, 325 (1993).
61. M. Gierlinski, *et al.*, *Mon. Not. R. Astron. Soc.* **288**, 958 (1997).
62. A. A. Zdziarski, J. Poutanen, W. S. Paciesas, L. Wen, *Astrophys. J.* **578**, 357 (2002).
63. V. Piirola, A. Berdyugin, S. Berdyugina, *Ground-based and Airborne Instrumentation for Astronomy V*, S. K. Ramsay, I. S. McLean, H. Takami, eds. (2014), vol. 9147 of *Proc. SPIE*, p. 91478I.
64. V. Piirola, I. A. Kosenkov, A. V. Berdyugin, S. V. Berdyugina, J. Poutanen, *Astron. J.* **161**, 20 (2021).
65. I. A. Kosenkov, *et al.*, *Mon. Not. R. Astron. Soc.* **468**, 4362 (2017).
66. Gaia Collaboration, *et al.*, *Astron. & Astrophys.* **649**, A1 (2021).
67. L. Lindgren, *et al.*, *Astron. & Astrophys.* **649**, A4 (2021).

68. K. Serkowski, *Advances in Astronomy and Astrophysics* **1**, 289 (1962).
69. M. J. Reid, *et al.*, *Astrophys. J.* **742**, 83 (2011).

Acknowledgements

The authors thank James Miller-Jones and Jerome Orosz for very helpful discussions of the optical constraints on the orbital inclination of Cyg X-1. The paper is based on the observations made by the Imaging X-ray Polarimetry Explorer (IXPE), a joint US and Italian mission. This research used data products provided by the IXPE Team (MSFC, SSDC, INAF, and INFN) and distributed with additional software tools by the High-Energy Astrophysics Science Archive Research Center (HEASARC), at NASA Goddard Space Flight Center (GSFC). We thank the *NICER*, *NuSTAR*, *INTEGRAL*, *Swift*, and *SRG/ART-XC* teams and Science Operation Centers for their support of this observation campaign.

Funding: The US contribution is supported by the National Aeronautics and Space Administration (NASA) and led and managed by its Marshall Space Flight Center (MSFC), with industry partner Ball Aerospace (contract NNM15AA18C). The Italian contribution is supported by the Italian Space Agency (Agenzia Spaziale Italiana, ASI) through contract ASI-OHBI-2017-12-I.0, agreements ASI-INAF-2017-12-H0 and ASI-INFN-2017.13-H0, and its Space Science Data Center (SSDC), and by the Istituto Nazionale di Astrofisica (INAF) and the Istituto Nazionale di Fisica Nucleare (INFN) in Italy. HK acknowledges NASA support under grants 80NSSC18K0264 and NNX16AC42G. MD and JS thank for the support from the GACR project 21-06825X and the institutional support from RVO:67985815. AV, JP and SST thank the Russian Science Foundation grant 20-12-00364 and the Academy of Finland grants 333112, 347003, 349144, and 349906 for support. AI acknowledges support from the Royal Society. POP thanks for the support from the High Energy National Programme (PNHE) of CNRS and from the French space agency (CNES). DB, SK, NM, RS acknowledge support from the European Research Council (ERC) under the European Unions Horizon 2020 research and innovation programme under grant agreement No. 771282. VK thanks Vilho, Yrjö and Kalle Väisälä Foundation. PT and JW acknowledge funding from Bundesministerium für Wirtschaft and Klimaschutz under Deutsches Zentrum für Luft- und Raumfahrt grant 50 OR 1909 I.A. acknowledges financial support from the Spanish "Ministerio de Ciencia e Innovación" (MCINN) through the "Center of Excellence Severo Ochoa" award for the Instituto de Astrofísica de Andalucía-CSIC (SEV-2017-0709) and through grants AYA2016-80889-P and

PID2019-107847RB-C44.

Author contributions: HK, Fabio Muleri, MD, AV, NRC, JS, AI, GM, JG, VL, and JP participated in the planning of the observation campaign and the analysis and modeling of the data; MN, TK, JR, and WZ contributed to the analysis or modeling of the data. AB, VK, SVB, MK, TS, DB, SK, NM, and RS contributed to the optical polarimetric data. JM and PD contributed the *Swift* results, JW and PT the *INTEGRAL* results, and AAL, SVM, and ANS the *SRG/ART-XC* results. SB, FC, NDL, LL, AM, TM, NO, AR, POP, PS, AFT, FT, MW, and SZ contributed to the discussion of the results. Frédéric Marin and SF served as internal referees. The other members of the *IXPE* collaboration contributed to the design of the mission and its science case and planning of the observations. All authors provided input and comments on the manuscript.

Competing interests: The authors declare no conflicts of interest.

Data and materials availability: IXPE data used in the analysis are available through the NASA data archive at <https://heasarc.gsfc.nasa.gov>.

Supplementary Materials for

Polarized X-rays Constrain The Disk-Jet Geometry in a Black Hole X-ray Binary

Henric Krawczynski *et al.*

Corresponding author: Henric Krawczynski, email: krawcz@wustl.edu

The PDF file includes:

Materials and Methods

Figures S1 to S9

Tables S1 to S4

References 41-69

Materials and Methods

Data Sets and Analysis Methods

The *IXPE* analysis is based on the level 2 *IXPE* data now publicly available in NASA’s HEASARC data archive¹. *IXPE* acquired 242 ksec of data between May 15, 2022 and May 21, 2022. The spectral fitting on *IXPE* data is equivalent to other X-ray observatories, and therefore it was carried out with standard software of the field, in particular, with the *XSPEC* (41) and *Sherpa* (42–45) packages. The model-independent Stokes parameter analysis (46) of the *IXPE* polarization data was performed with custom-software developed for *IXPE* (47). Confidence region for the polarization measurements were calculated following standard practices (48, 49). The results were cross-checked by fitting the Stokes *I*, *Q* and *U* data with *XSPEC* using the response matrices from NASA’s HEASARC data archive (50). The analysis selects source and background data based on the reconstructed arrival direction in celestial coordinates. The former is picked out in a circular region of ~ 80 arcsec radius, and the latter as a concentric annulus of inner and outer radius equal to ~ 150 and ~ 310 arcsec, respectively. We use the additive property of the Stokes parameters to subtract the background, which is at least a factor 70 smaller than the signal in any of the energy intervals that we considered for polarization measurement.

NuSTAR acquired a total of 42 ksec of data between May 18 and May 21, 2022. The *NuSTAR* data were processed with the *NuSTARDAS* software (version v1.9.7) of the *HEASOFT* package (version v6.30.1).

NICER acquired a total of 87 ksec of data between May 15 and May 21, 2022. The *NICER* data were processed with the *NICERDAS* software (version v9.0) of the *HEASOFT* package (version v6.30.1).

Swift observed Cyg X-1 daily between May 15 and May 20, 2022 for a total of ~ 54 ksec, with the XRT instrument operating in Windowed Timing (WT) mode. The observations were processed using the tools in *HEASOFT* v6.30. The initial event cleaning was performed using *XRTPIPELINE*, the spectra and lightcurves were extracted using *XSELECT*, and ancillary response files (ARF) were generated using *XRTMKARF*.

¹<https://heasarc.gsfc.nasa.gov/docs/heasarc/missions/ixpe.html>

The Mikhail Pavlinsky ART-XC telescope (51) on board the *SRG* observatory (52) carried out two simultaneous with *IXPE* observations of Cyg X-1 on 2022 May 15-16 and 18-19 with 86 and 85 ks exposures, respectively. ART-XC data were processed with the analysis software ARTPRODUCTS v0.9 with CALDB version 20200401.

INTEGRAL collected data on Cyg X-1 between May 15 and May 20, 2022 with a total exposure time of ~ 196 ksec. *INTEGRAL*/ISGRI lightcurves were generated using version 11.2 of the Off-line Scientific Analysis (OSA) software.

Overall lightcurves

Figure S1 shows the *IXPE*, *SRG*/ART-XC, *NICER*, *NuSTAR* and *INTEGRAL* lightcurves. The spectropolarimetric analysis uses the intersection of the observation time intervals (good time intervals, or GTIs) of the three missions (*IXPE*, *NICER*, and *NuSTAR*). A detailed analysis of the *IXPE* Stokes Q and U lightcurves will be presented in a forthcoming paper.

Detailed *IXPE* Polarization Results

Figure S2 shows the *IXPE* polarization signal in terms of the normalized Stokes parameters Q/I and U/I , giving the polarized beam intensity along the north-south ($Q/I > 0$) and east-west ($Q/I < 0$) directions as well as along the northeast-southwest ($U/I > 0$) and northwest-southeast ($U/I < 0$) directions. Tables S1 and S2 give the results of both analyses in terms of the Stokes parameters, and polarization degrees and angles, respectively.

We studied the energy dependence of the polarization degree by fitting constant and linear polarization degree models to the data, see Figure S3. The constant dependence fit gives a polarization degree $= (4.29 \pm 0.18)\%$ with $\chi^2/\text{d.o.f} = 18.61/10$ and null hypothesis probability of 0.0455 with 10 degrees of freedom. The best linear dependence fit gives a polarization degree $= A + B \times (E/\text{keV} - 1)$ with $A = (2.9 \pm 0.4)\%$ and $B = (0.58 \pm 0.15)\%$ with $\chi^2/\text{d.o.f} = 3.96/9$ and null hypothesis probability of 0.914 with 9 degrees of freedom. Thus there is an indication that the polarization degree grows with energy. This is also supported by the fact that the first four low energy bins are all below constant energy dependence fit while for all larger energy bins they are above. If we perform the same analysis for the polarization angle, we get polarization angle $= -20.7 \pm 1.2^\circ$ with $\chi^2/\text{d.o.f} = 8.55/10$ and null hypothesis probability of

0.575 with 10 degrees of freedom for a constant dependence, and polarization angle= $A + B \times (E/\text{keV} - 1)$ with $A = -15.8 \pm 2.6$ and $B = -1.80 \pm 0.86$ with $\chi^2/\text{d.o.f} = 4.19/9$ and null hypothesis probability of 0.898 with 9 degrees of freedom for a linear dependence.

Figure **S3** shows apparent drops of the 4.5 – 5 keV and 6 – 6.5 keV polarization degrees. We find however, that these drops are not statistically significant. Moreover, based on the constraints on the equivalent width of the fluorescent Fe $K\alpha$ -line from the spectral analysis of the *NICER* and *NuSTAR* data, we find that the maximum possible Fe $K\alpha$ depolarization is much smaller than the observed fluctuation.

The lightcurves in Figure **S1** show that the Cyg X-1 *IXPE* count rates varied between 20 and 80 cts/s. We studied the flux dependence of the polarization properties by analyzing a low-count rate data set (<45 cts/sec) and a high-flux data set when the flux consistently exceeded 45 cts/sec (2022-05-18 02:47:49.684 – 2022-05-21 07:31:05.743). The energy-resolved polarization degrees and polarization angles are shown in Fig. **S4**. There is no clear evidence for a change of the polarization degrees or angles. If the flux changes are entirely due to absorption, the absorber has to cover all emitting regions simultaneously. This finding rules out scenarios in which the polarized signal stems from a much larger emission region, e.g., the jet outside of the region covered by the absorber.

IXPE, NICER and NuSTAR energy spectra

As a demonstration of a spectropolarimetric analysis, we present here the results from fitting a simple model to the broadband Stokes I spectrum provided by *NICER*, *NuSTAR* and *IXPE* and the Stokes Q and U spectra provided only by *IXPE*. We use the data from the first *NuSTAR* observation and the simultaneously acquired *NICER* data, to eliminate differences due to spectral variability. We use the entire *IXPE* observation to maximize the signal-to-noise ratio. We fit the two *NuSTAR* Focal Plane Modules (FPMs) and the three *IXPE* DUs separately in the fit. For the Stokes I spectrum, we employ the model

$$\text{MBPO} * \text{TBABS} * (\text{DISKB} + \text{XILLVERCP} + \text{RELXILLCP} + \text{NTHCOMP}). \quad (\text{S1})$$

Here DISKB represents thermal disk emission and NTHCOMP represents Comptonized emission observed directly from the corona. The RELXILLCP component represents coronal X-rays

that are reflected from the inner accretion disk and distorted by relativistic effects. The XILLVERCP component represents coronal X-rays that are reflected from the outer disk and the companion star and not subject to strong relativistic effects. TBABS accounts for line-of-sight absorption by the interstellar medium.

The model MBPO is included to account for cross-calibration discrepancies we encountered between the three observatories. It multiplies the model spectrum by a broken power law, $MBPO(E) = N(E/E_{br})^{\Delta\Gamma}$, where $\Delta\Gamma = \Delta\Gamma_1$ for $E < E_{br}$ and $\Delta\Gamma = \Delta\Gamma_2$ for $E \geq E_{br}$. For *NICER*, we fix the power-law indices to zero and the normalization to unity. For *NuSTAR*, we tie $\Delta\Gamma_2 = \Delta\Gamma_1$ (i.e. employing only a single power law) but leave $\Delta\Gamma_1$ and N as free parameters for each FPM. For the *IXPE* DUs, we must leave all MBPO parameters free to achieve an acceptable fit. We also include a 0.5% systematic error to further account for cross-calibration discrepancies. Finally, the *NuSTAR* FPM A disagrees with the FPM B and *NICER* in the 3-4 keV band, and *IXPE* DU3 disagrees with all other instruments (even with the use of MBPO) in the > 5 keV energy range, and so we ignore these ranges in our fit.

We first fit jointly to the *NICER* and *NuSTAR* data, then add *IXPE* Stokes I to the fit before finally adding *IXPE* Stokes Q and U . At each stage, the best-fitting parameters do not change significantly. The top panel of Fig S5 shows the best-fitting model and the data ‘unfolded’ around that model. The separate spectral components are shown in the top plot: DISKBB (dashed), XILLVERCP (dotted), RELXILLCP (dash-dotted) and NTHCOMP (dash-triple-dotted). The direct coronal emission (NTHCOMP) dominates the 2–8 keV flux (88.9%). The DISKBB, XILLVERCP and RELXILLCP components contribute respectively 0.57%, 0.50% and 10.05% of the flux. The fractional contribution of each model component is consistent whether we consider only *NICER* and *NuSTAR* or also include *IXPE*. Since the direct coronal flux dominates the 2–8 keV flux, it must also dominate the polarization. For instance, the relativistic reflection component would need to be $\sim 40\%$ polarized to achieve the observed overall polarization of $\sim 4\%$. However, the reflected emission exhibits most likely much smaller polarization degrees. In the case of the reflection of unpolarized X-rays off neutral accretion disks this was shown in (53). We have extended these studies for the case of the reflection of unpolarized X-rays off ionized accretion disks making use of the polarized reflection tables from (54) (publication in preparation). Our studies over a broad range of different parameters show that the 2-8 keV

emission exhibits overall polarization degrees well below those required here, as the polarization of the emission from different parts of the accretion disk cancel. We find similar results for the reflection of unpolarized X-rays off truncated disks.

As a simple ‘toy’ model, we therefore assign a constant (independent of energy) polarization degree and angle to the NTHCOMP component (the model POLCONST) and assume that the other components are unpolarized. The middle panel of Fig S5 shows the resulting fit to *IXPE* Stokes Q (blue circles) and Stokes U (magenta squares). We achieve a good overall fit with a reduced χ^2 of $\chi^2/\text{dof} = 2380.4/2415$. The bottom panel shows the contributions from each energy channel to χ , demonstrating that there are no structured residuals. The best-fitting polarization degree and angle of the corona from this simple model are respectively $3.63 \pm 0.26\%$ and -20.5 ± 2.1 (90% confidence).

Model constraints on the inclination of the inner accretion disk

We studied the energy spectra and polarization properties of different corona shapes and properties with ray tracing codes. We show here exemplary simulation results that match the *IXPE*, *NICER*, and *NuSTAR* energy spectra qualitatively, and present the predicted polarization properties.

We used the general relativistic ray tracing code `kerRC` (14) to evaluate the polarization that cone-shaped coronae centered on the BH spin axes and wedge-shaped coronae sandwiching the accretion disk can produce. The code assumes a standard geometrically thin, optically thick accretion disk extending from the innermost stable circular orbit to 100 gravitational radii $r_g = GM/c^2$ with G being the gravitational constant, M the BH mass, and c the speed of light. The code uses Monte Carlo methods to simulate the emission of the accretion disk photons, the polarization-changing Comptonization of the photons in the corona, and the reflection of the photons off the accretion disk adopting the `XILLVER` reflection model for the reflected intensity (55–57), and Chandrasekar’s analytical solution for the reflected polarization (58).

In both cases, we chose corona parameters which maximize the predicted polarization degrees, i.e., cone-shaped coronae very close to the accretion disk, and rather thin wedge-shaped coronae with a half opening angle of 10° . The model parameters are given in Table S3.

For both models, the statistical errors on the Stokes U parameter (due to photon counting

noise in the Monte Carlo simulation) are appreciable, because most positive and negative U contributions cancel, leaving a highly fluctuating residual. The statistical errors also increase for energies $\gg 10$ keV where the number of simulated photons contributing to the results becomes small. The left panel of Figure **S6** presents results for a flat wedge-shaped sandwich corona. The polarization degree rises from 4% at 2 keV to 6% at 8 keV, and the polarization direction is perpendicular to the accretion disk plane at all energies. The right panel of Figure **S6** shows the results for a cone-shaped corona close to the spin axis. The predicted polarization degrees are 4–6% over the *IXPE* energy band but the polarization direction is parallel to the accretion disk plane. For smaller inclinations (e.g. 75° , not shown here) the polarization degrees drop well below 4% and the polarization exhibits a swing in the *IXPE* energy band. We used the general relativistic ray tracing code *MONK* (13) to study if coronae moving radially away from the black hole with relativistic speeds, coronae at different heights above the BH, or the reflection off truncated accretion disks can produce higher polarization degrees, but without success. For coronae very close to the black hole, the polarization direction becomes perpendicular to the disk plane, but the polarization degrees are smaller than observed and tend to decrease with energy from 2 keV to 8 keV. Although some coronae moving relativistically away from the BH along the spin axis (e.g., (59)) produce $>4\%$ polarization degrees for $i \approx 30^\circ$, they do not present viable configurations as the predicted polarization is parallel to the accretion disk plane.

We studied the polarization of the truncated disk/inner hot flow scenario using the formalism described in (11). The code treats Compton scattering of polarized radiation in a plane-parallel geometry in flat space. It uses exact Compton scattering redistribution matrices for isotropic electrons (60) and solves the polarized radiation transfer equations using an expansion of the intensities in scattering orders. We do not include reflection off the cold disk (16) in the results presented here to avoid uncertainties related to the properties of the reflecting plasma.

Fig. **S7** shows the resulting spectra (panels A and C) and polarization (panels B and D) of a truncated disk/inner hot flow model. The code simulates a plane parallel slab corona, using a prescription to inject seed photons that mimics the truncated disk scenario. Panels A and B correspond to the case of seed photons coming from the disk, seen at an inclination of 30° and 47° . The electron temperature is assumed to be $kT_e = 100$ keV, the seed blackbody temperature $kT_{\text{bb}} = 0.1$ keV and the Thomson optical depth $\tau_T = 1.0$ (61, 62). The predicted

polarization degrees are between 1.5% and 4.2%, for $i = 30^\circ$ and 47° , respectively, and the polarization direction is orthogonal to the accretion disk plane. Panels C and D of Fig. S7 illustrate the results for the case of synchrotron seed photons; other parameters are the same as in the previous case. The synchrotron emission has a peak at energies $\sim 1 - 10$ eV, much lower than corresponding peak of the disk photons, hence we see only high scattering orders in the *IXPE* band. This implies that the dependence of polarization degree on energy is mostly washed out, and the polarization degree is nearly constant: $\sim 2.5\%$ and 5% for $i = 30^\circ$ and 47° , respectively.

Optical polarimetry

The optical polarimetric observations were performed using DIPol-2 polarimeter, installed on the remotely operated Tohoku 60 cm (T60) telescope at the Haleakala Observatory, Hawaii. DIPol-2 is a double-image CCD polarimeter, capable of measuring linear and circular polarization in three (*BVR*) optical filters simultaneously (63, 64). The design of this instrument optically eliminates the sky polarization (even if it is variable), which results in a high (up to 10^{-5}) polarimetric precision. The instrumental polarization is below the 10^{-4} level and measured by observing twenty unpolarized nearby stars. The zero point of the PA was determined by observing two highly polarized standard stars (HD204827 and HD25443).

We observed Cyg X-1/HDE 226868 for five nights during the week 2022 May 15–21 for about 4 hours each night. One measurement of Stokes parameters took about 20 s and we obtained 2298 individual measurements of the normalized Stokes q_{obs} and u_{obs} parameters simultaneously in three filters (*BVR*). These individual measurements were used to compute average intranight values of Stokes parameters using the 2σ weighting algorithm (64, 65). The error on the final average corresponds to the standard deviation of individual measurements resulting from the orbital variability of the source.

The polarization produced by the interstellar (IS) medium has been estimated by observing a sample of field stars (see Fig. S8), which are close in distance to the target as indicated by their Gaia parallaxes (see Fig. S9) (66, 67). Taking into account angular separation on the image, closeness in distance, and the wavelength dependence of the polarization, we choose two stars (Ref 1 and Ref 2) from our sample as the IS polarization standards. We have considered two

cases: when the Stokes parameters of the IS polarization were set to be equal to those of Ref 2 and to the weighted average of those of Ref 1 and Ref 2. For both cases, the normalized Stokes parameters (q_{is} , u_{is}) were subtracted from the measured values of Stokes parameters of the target to obtain the intrinsic polarization (q_{int} , u_{int}) estimates. From this we get the intrinsic polarization degree (PD) and polarization angle (PA) as

$$PD = \sqrt{q_{int}^2 + u_{int}^2}, \quad PA = \frac{1}{2} \text{atan2}(u_{int}/q_{int}). \quad (\text{S2})$$

The uncertainty on the polarization degree $\Delta(PD)$ was estimated as the uncertainty of the individual Stokes parameters, and includes both the source and IS polarization errors. The uncertainty on the polarization angle (in radians) was estimated as $\Delta(PA) = \Delta(PD)/(2 PD)$ (68). The observed normalized Stokes parameters, the IS polarization and the intrinsic Stokes parameters as well as the polarization degrees and angles are reported in Table S4.

We used the RoboPol polarimeter in the focal plane of the 1.3 m telescope of the Skinas observatory (Greece) to obtain additional *R*-band polarimetry. The observations were performed between 5/13/2022 and 6/2/2022 with multiple pointings in 10 nights. In total, 21 exposures series were acquired, each series consisting of 10 to 20 1-2 sec shots. The instrumental polarization was found with a set of unpolarized standard stars (BD+28.4211, BD+33.2642, BD+32.3739, BD+40.2704, HD154892). The zero position angle was determined based on three highly polarized standard stars (VI Cyg 12, Hiltner 960 and CygOB2 14). The Cyg X-1/HDE 226868 measurements do not reveal any polarization variability exceeding that of the standard stars ($\sigma_q = 0.12\%$, $\sigma_u = 0.08\%$). We determined the average polarization parameters of Cyg X-1/HDE 226868 from calculating the sigma-clipped median of the relative Stokes parameters. The uncertainties were determined by error propagation adding the instrumental polarization uncertainties in quadrature. We determined the intrinsic source polarization by subtracting the IS polarization using the Ref 2 star mentioned above (see Table S4).

We find polarization angles of Cyg X-1/HDE 226868 between -37° to -11° , close to the position angle of the jet from radio interferometry (from -26° to -9°) (4, 69). We note that the blue supergiant HDE 226868 companion star dominates the optical emission (21). The optical polarization is likely produced by the scattering of the stellar radiation off the bulge formed by the accretion stream interacting with the accretion disk (27).

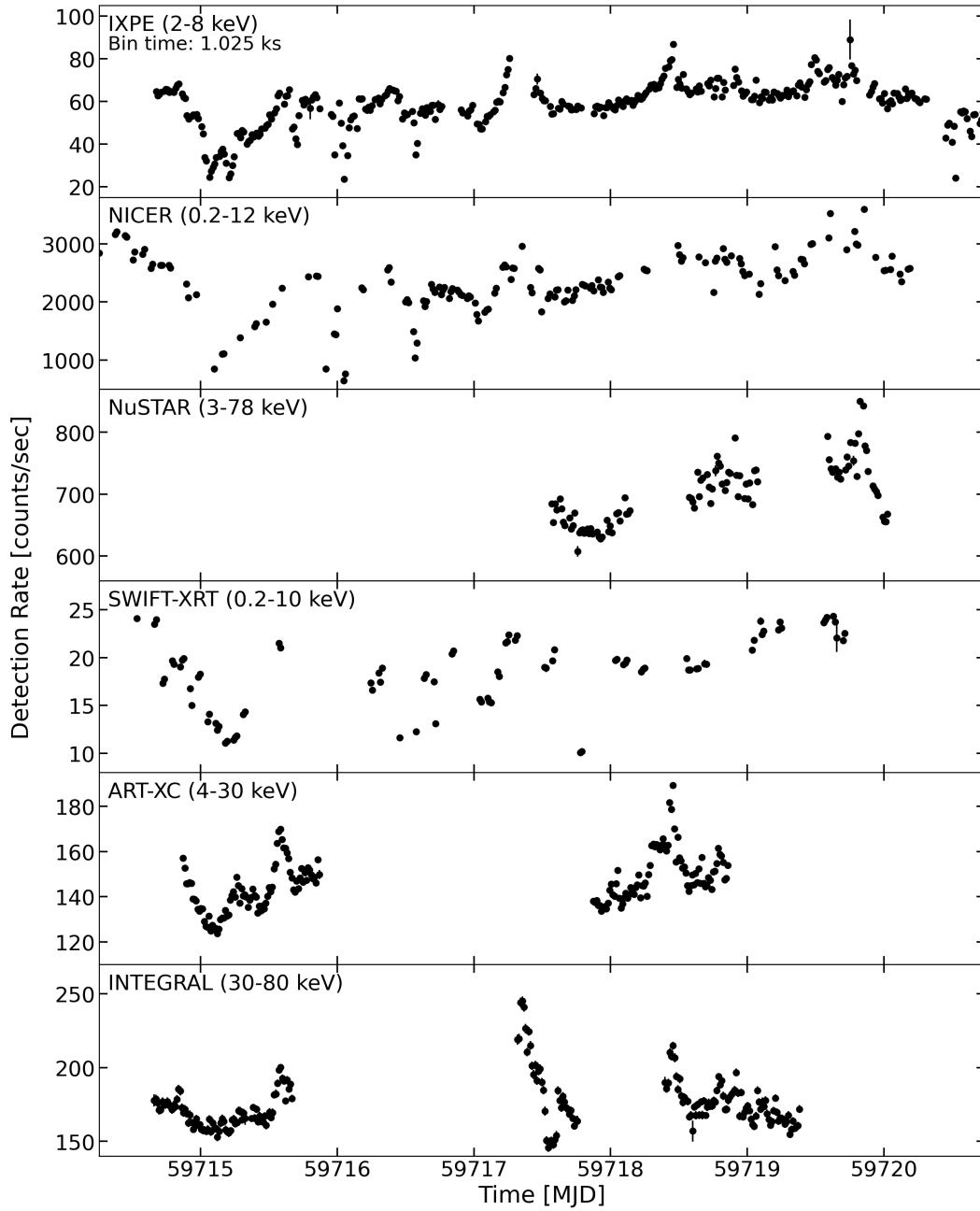


Figure S1: X-ray lightcurves of Cyg X-1. From top to bottom: *IXPE* (2–8 keV), *NICER* (0.2–12 keV), *NuSTAR* (3–78 keV), *Swift-XRT* (0.2–10 keV), *SRG/ART-XC* (4–30 keV), and *INTEGRAL* (30–80 keV) lightcurves. MJD 59715 is May 16, 2022.

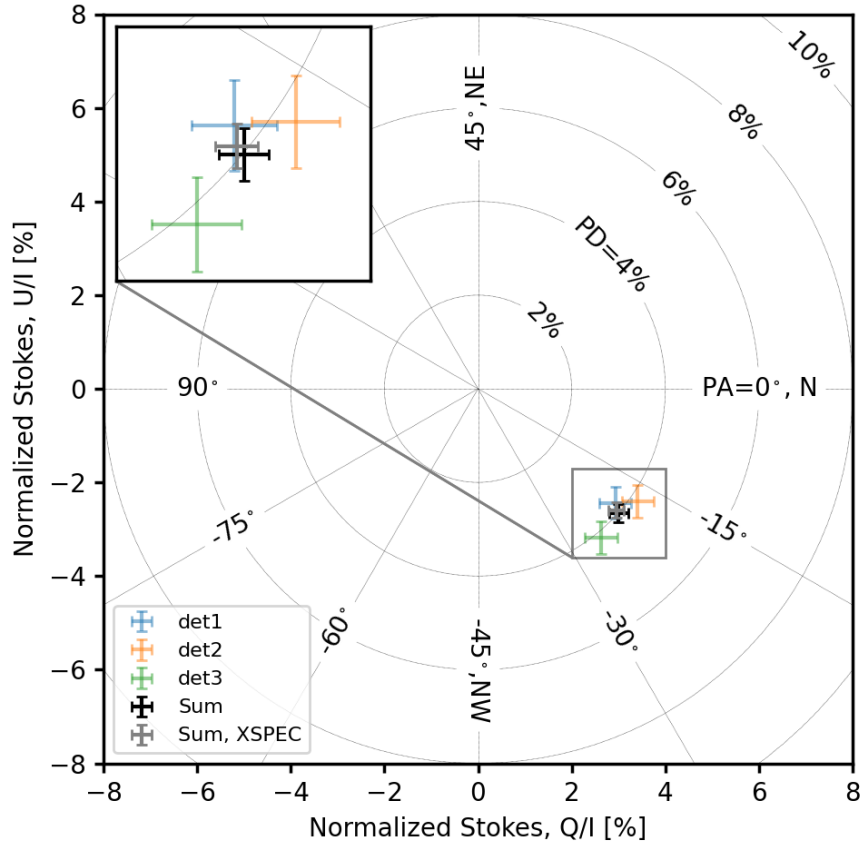


Figure S2: X-ray linear polarization of Cyg X-1. The linear polarization of the X-rays from the BH X-ray binary Cyg X-1 is shown at the plane of the normalized Stokes Q/I and U/I parameters measured with each of the three *IXPE* X-ray telescopes, and for the combined signal from all three telescopes. The circles give the contour of constant polarization degree (PD) while the radial lines correspond to constant polarization angle (PA). The error bars are 1σ .

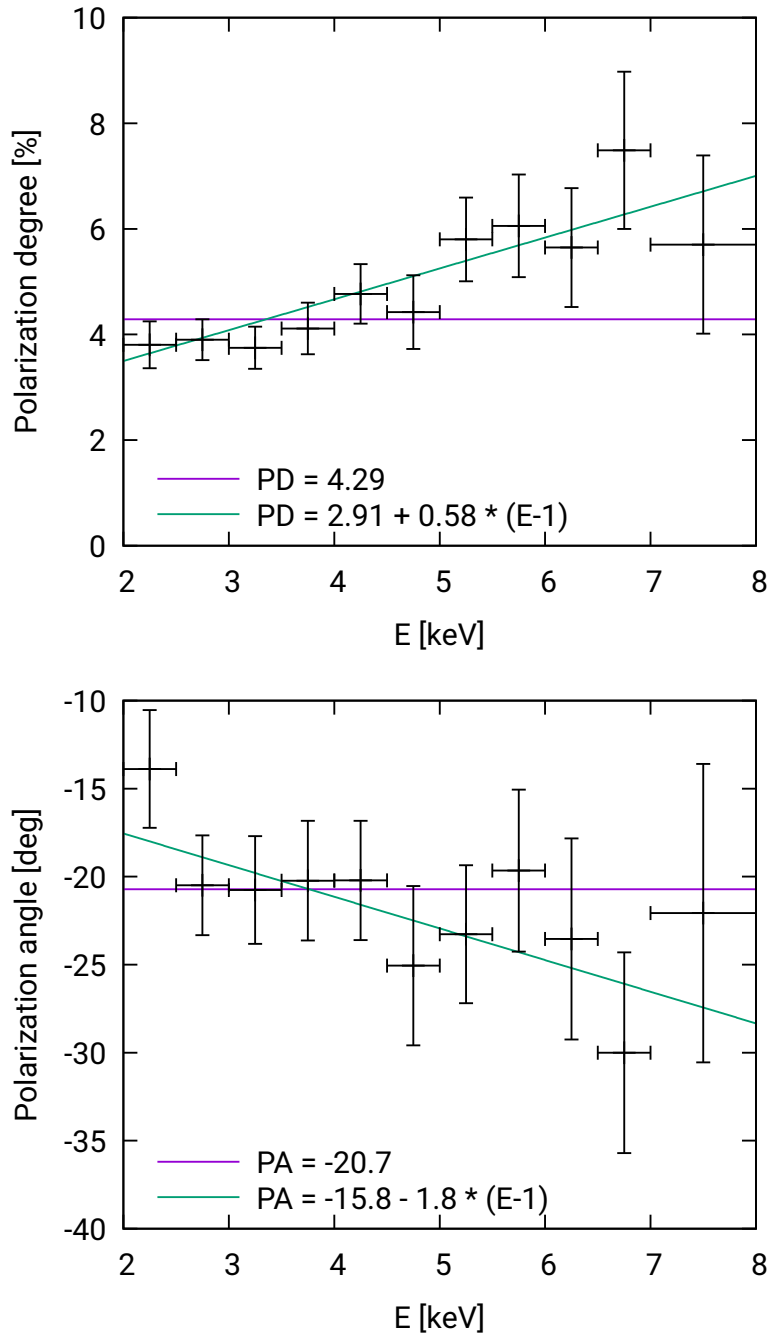


Figure S3: The energy dependence of the observed polarization degree (top) and polarization angle (bottom). The data (black crosses with 1σ errorbars) are produced by PCUBE algorithm of `xpbin` and summed for all detector units. The constant (violet) and linear (green) fits are also depicted (see the text for more details).

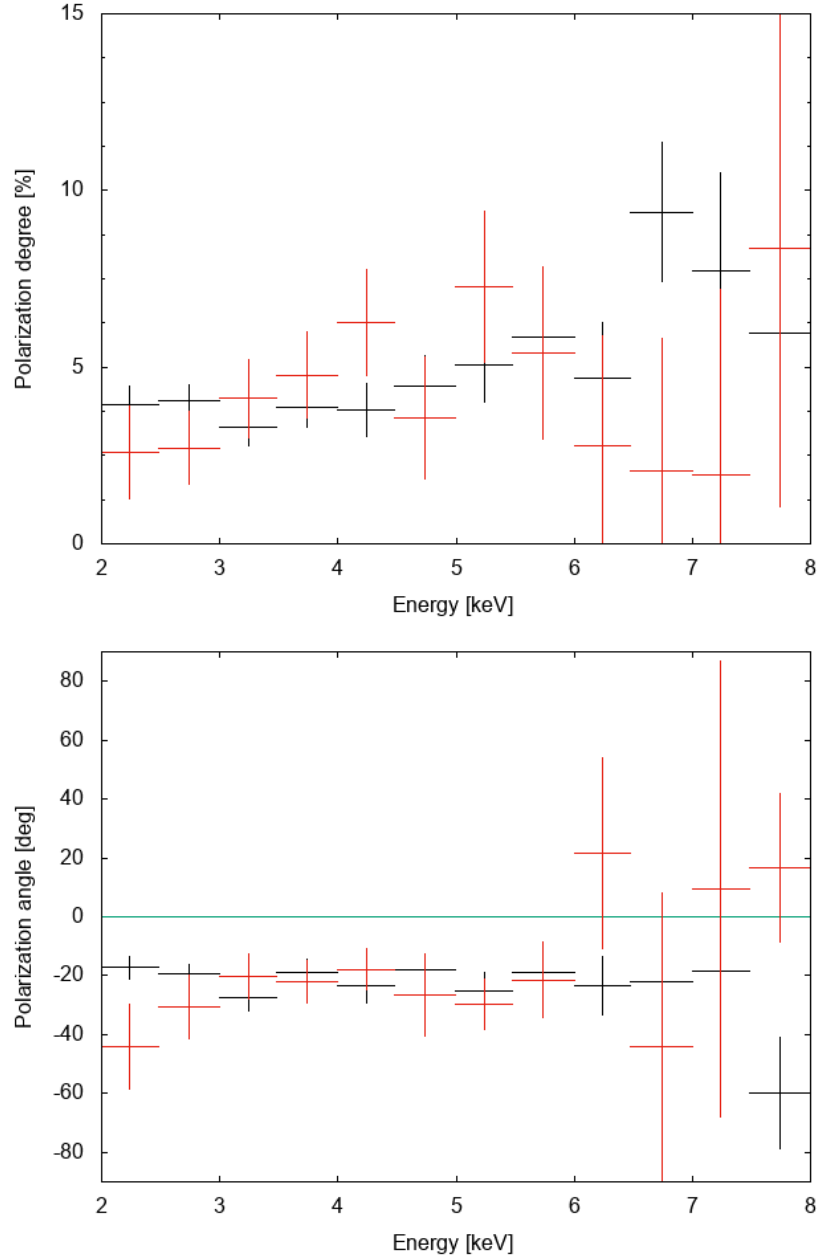


Figure S4: Polarization of Cyg X-1 at different flux levels. Comparison of the polarization degree (top) and polarization angle (bottom) in high-flux (black) and low-flux period (red) of Cyg X-1 selected from the *IXPE* lightcurve in Fig. S1. Top: polarization degree measurement. Bottom: polarization angle measurement.

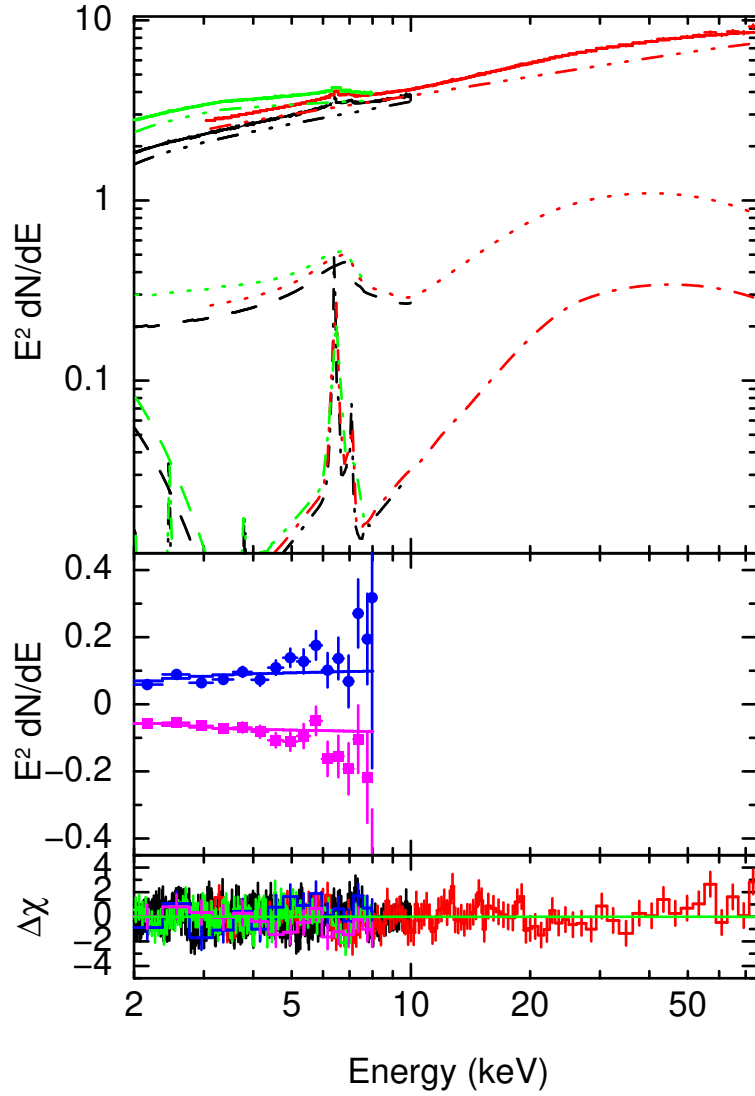


Figure S5: Results of spectropolarimetric fitting. The top panel is the X-ray spectrum (Stokes I). The solid lines represent the total model and the points are the data unfolded around the best-fitting model in units of $\text{keV cm}^{-2} \text{s}^{-1}$. Black, red and green colours represent *NICER*, *NuSTAR* and *IXPE* respectively. The middle panel shows Stokes Q (blue circles) and U (magenta squares), again unfolded around the best-fitting model and in units of $\text{keV cm}^{-2} \text{s}^{-1}$. The bottom panel shows residuals (contributions to χ). For plotting purposes only, data from different detectors of the same observatory have been grouped together, and a maximum of 10 energy channels have been grouped together to achieve a signal-to-noise ratio of 150 (the XSPEC command `setplot rebin 150.0 10`).

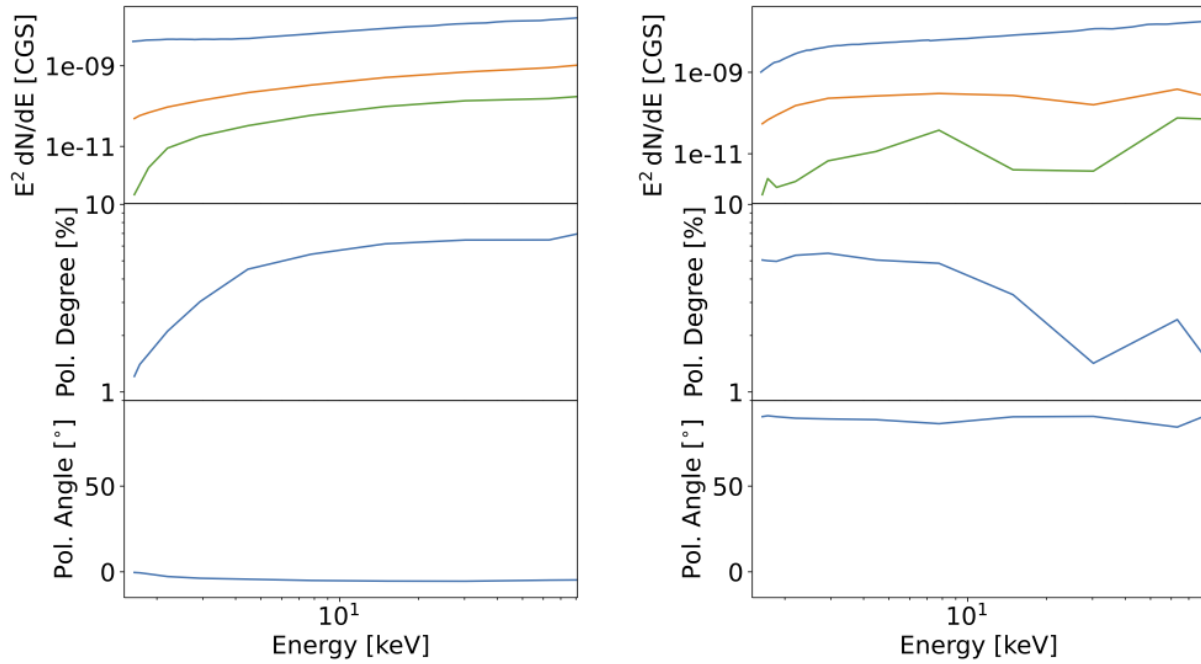


Figure S6: Polarimetric properties of the wedge- and cone-shaped corona models. From top to bottom: Predicted spectral energy distribution (SED), polarization degree and angle for the wedge-shaped (left) and cone-shaped (right) corona model (see text for details). The top panel shows from top to bottom Stokes I , and the absolute values of Stokes Q and U . For clarity, the figures show the results assuming the projection of the black hole spin onto the plane of the sky axis points due north ($Q/I=1$).

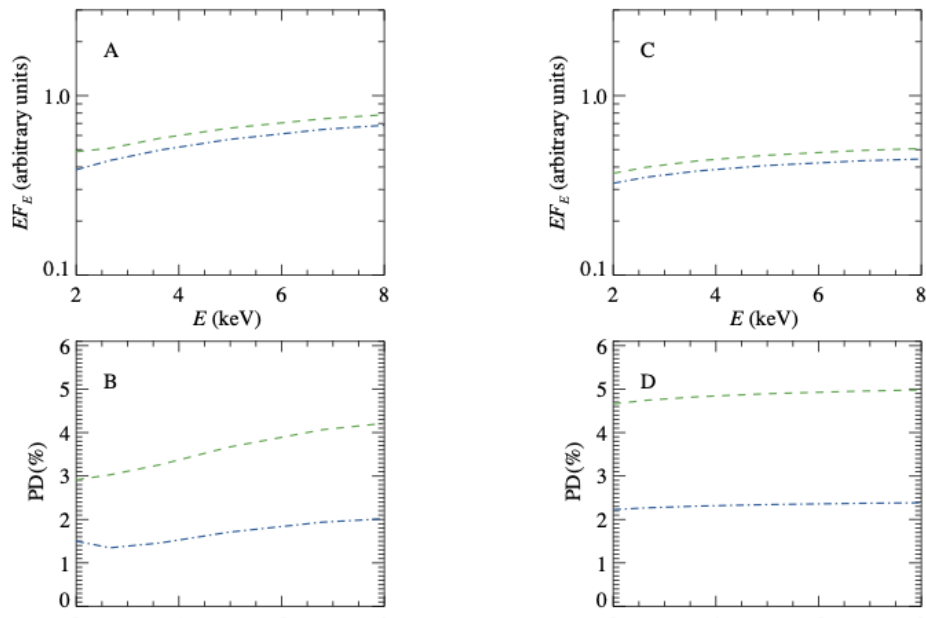


Figure S7: Spectra and polarization degree for the truncated disk and the inner hot flow geometry. (A) Spectrum and (B) polarization degree for the case where seed photons come from the outer cool accretion disk. (C) Spectrum and (D) polarization degree for the case for synchrotron seed photons. The polarization is parallel to the axis normal to the flattened hot medium (disk plane). Blue dot-dashed and green dashed lines correspond to the inclinations of the hot flow $i = 30^\circ$ and 47° , respectively.

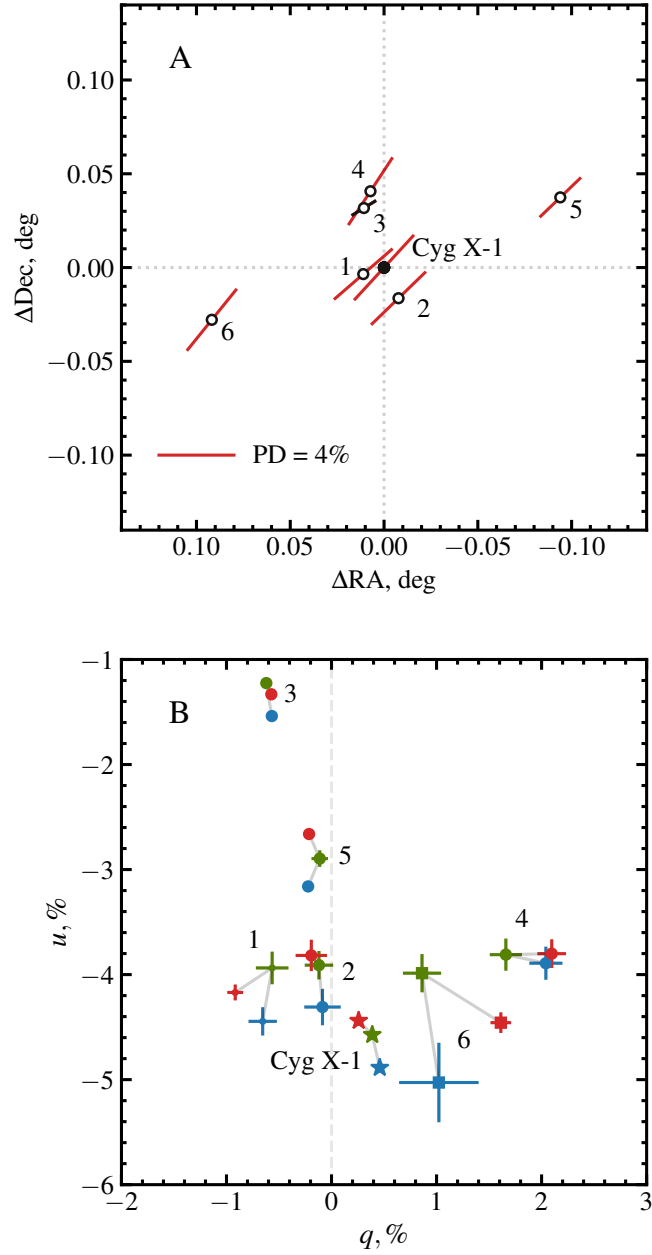


Figure S8: Polarization of nearby field stars around Cyg X-1. (A) Polarization vectors of the field stars (open circles) and Cyg X-1 (filled circle) in the B -filter. (B) The observed normalized Stokes parameters q and u for the field stars and Cyg X-1 (stars). Blue, green and red colors correspond to BVR filters, respectively. Errors are 1σ .

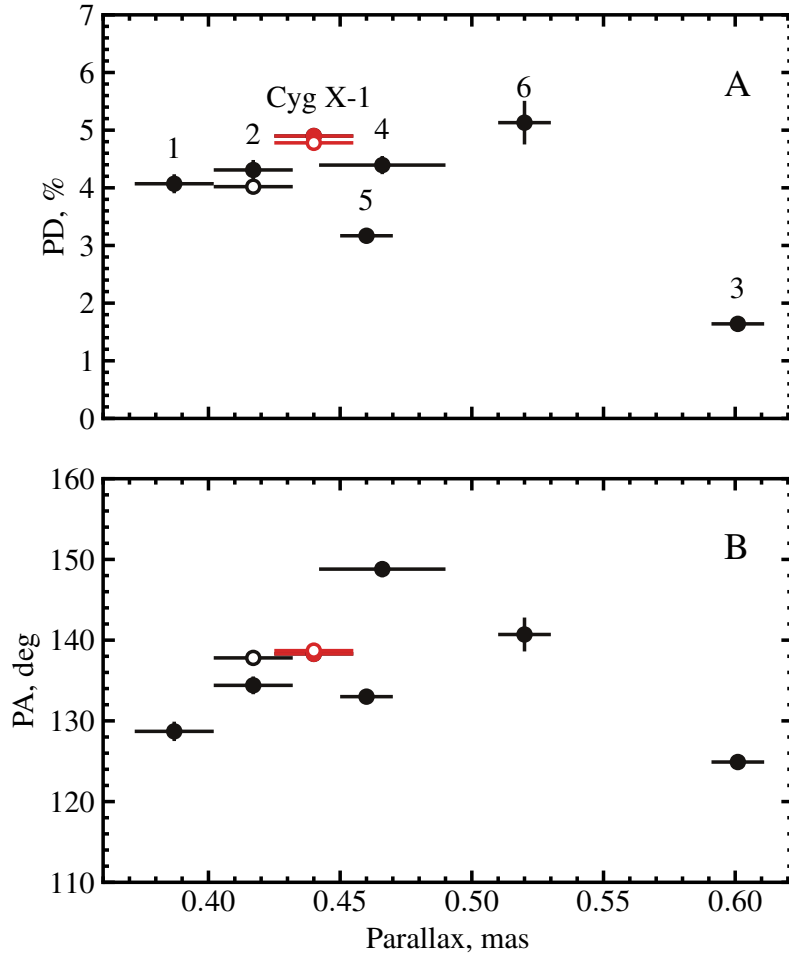


Figure S9: Polarization of nearby field stars around Cyg X-1 as a function of parallax. (A) PD and (B) PA for a set of field stars and Cyg X-1 as measured with DIPol-2 (filled circles) and RoboPol (open circles) in the *R*-band. The errors are given at the 1σ confidence level.

	2.0–3.0 keV	3.0–4.0 keV	4.0–6.0 keV	6.0–8.0 keV	2.0–8.0 keV
Q/I - det1 [%]	2.9 ± 0.5	2.5 ± 0.5	3.4 ± 0.6	3.0 ± 1.4	2.9 ± 0.3
Q/I - det2 [%]	3.3 ± 0.5	2.5 ± 0.5	3.9 ± 0.6	4.7 ± 1.4	3.4 ± 0.3
Q/I - det3 [%]	2.1 ± 0.5	2.7 ± 0.5	3.1 ± 0.6	3.4 ± 1.6	2.6 ± 0.4
Q/I - sum [%]	2.8 ± 0.3	2.5 ± 0.3	3.5 ± 0.3	3.7 ± 0.8	3.0 ± 0.2
Q/I - sum (XSPEC) [%]	2.9 ± 0.3	2.7 ± 0.3	3.4 ± 0.3	3.7 ± 0.8	2.9 ± 0.2
U/I - det1 [%]	-2.1 ± 0.5	-1.9 ± 0.5	-2.8 ± 0.6	-4.2 ± 1.4	-2.4 ± 0.3
U/I - det2 [%]	-1.3 ± 0.5	-2.3 ± 0.5	-2.7 ± 0.6	-6.0 ± 1.4	-2.4 ± 0.3
U/I - det3 [%]	-2.9 ± 0.5	-2.9 ± 0.5	-4.0 ± 0.6	-2.9 ± 1.6	-3.2 ± 0.4
U/I - sum [%]	-2.1 ± 0.3	-2.3 ± 0.3	-3.1 ± 0.3	-4.5 ± 0.8	-2.7 ± 0.2
U/I - sum (XSPEC) [%]	-2.3 ± 0.3	-2.4 ± 0.3	-3.2 ± 0.3	-4.2 ± 0.8	-2.6 ± 0.3

Table S1: *IXPE* polarization results in terms of the Stokes parameters from the *ixpeobssim* (top) and XSPEC(bottom) analysis. The two methods and the independent analysis of single *IXPE* telescopes provides statistically consistent results. The uncertainties are quoted for a 68.3% confidence interval, assuming that the Stokes parameters are independent.

	2.0–3.0 keV	3.0–4.0 keV	4.0–6.0 keV	6.0–8.0 keV	2.0–8.0 keV
PD - det1 [%]	3.5 ± 0.5	3.1 ± 0.5	4.4 ± 0.6	5.1 ± 1.4	3.8 ± 0.3
PD - det2 [%]	3.6 ± 0.5	3.4 ± 0.5	4.7 ± 0.6	7.6 ± 1.4	4.2 ± 0.3
PD - det3 [%]	3.6 ± 0.5	3.9 ± 0.5	5.1 ± 0.6	4.5 ± 1.6	4.1 ± 0.4
PD - sum [%]	3.5 ± 0.3	3.5 ± 0.3	4.7 ± 0.3	5.8 ± 0.8	4.0 ± 0.2
PD - sum (XSPEC) [%]	3.7 ± 0.3	3.6 ± 0.3	4.7 ± 0.3	5.6 ± 0.8	3.9 ± 0.2
PD S/N	13σ	12σ	14σ	7σ	20σ
PA - det1 [deg]	-18 ± 4	-19 ± 4	-20 ± 4	-27 ± 8	-20 ± 3
PA - det2 [deg]	-11 ± 4	-22 ± 4	-17 ± 4	-26 ± 5	-18 ± 2
PA - det3 [deg]	-27 ± 4	-23 ± 4	-26 ± 4	-20 ± 10	-25 ± 2
PA - sum [deg]	-18 ± 2	-21 ± 2	-21 ± 2	-25 ± 4	-21 ± 1
PA - sum (XSPEC) [deg]	-19 ± 2	-21 ± 2	-21 ± 2	-25 ± 4	-21 ± 1

Table S2: Same as Table S1, but for the polarization degrees and angles. Also in this case, quoted uncertainties are at 68.3% confidence level and they are calculated assuming that the polarization degree and polarization angle are independent. The significance of the measurement is approximately the measured polarization degree divided by the uncertainty shown in the table, for the sum of the three *IXPE* telescopes.

Parameter	Symbol	Unit	wedge	cone
Black hole spin	a	none	0.9	0.9
Black hole mass	M	M_{\odot}	21.2	same
Corona temperature	T_{C}	keV	250	150
Optical depth	τ_{C}	none	0.122	0.79
Opening angle	θ_{C}	deg	10	25
Corona inner/outer edge	r_1, r_2	r_{g}	2.32–100	2.5–20
Inclination	i	deg	65	85
Accretion rate	\dot{M}	10^{18} g s^{-1}	0.075	0.1
Cyg X-1 distance	d	kpc	2.22	same
Assumed pol. direction	ψ	deg	0	0
XILLVER metal abundance	A_{Fe}	solar	1	1
XILLVER electron temperature	$k_{\text{B}} T_{\text{e}}$	keV	same as T_{C}	same as T_{C}
XILLVER e^{-} -density in cm^{-3}	$\log_{10}(n_{\text{e}})$	none	17.5	17.7
Equivalent hydrogen column	N_{H}	10^{22} cm^{-2}	0.8	4

Table S3: `kerrC` model parameters used for Figure S6.

Band	B		V		R	
	q (%)	u (%)	q (%)	u (%)	q (%)	u (%)
Observed polarization of Cyg X-1/HDE 226868						
DIPol-2	0.46 ± 0.06	-4.89 ± 0.04	0.39 ± 0.04	-4.57 ± 0.04	0.26 ± 0.03	-4.44 ± 0.03
RoboPol	–	–	–	–	0.61 ± 0.13	-4.74 ± 0.12
Interstellar polarization						
Ref 2/DIPol-2	-0.09 ± 0.17	-4.31 ± 0.17	-0.12 ± 0.14	-3.91 ± 0.14	-0.19 ± 0.15	-3.82 ± 0.15
Ref 1+2/DIPol-2	-0.41 ± 0.11	-4.39 ± 0.11	-0.33 ± 0.10	-3.92 ± 0.10	-0.67 ± 0.07	-4.05 ± 0.07
Ref 2/RoboPol	–	–	–	–	0.39 ± 0.16	-4.00 ± 0.08
Intrinsic polarization of Cyg X-1/HDE 226868						
Ref 2/DIPol-2	0.55 ± 0.17	-0.58 ± 0.17	0.51 ± 0.14	-0.66 ± 0.14	0.45 ± 0.15	-0.62 ± 0.15
Ref 1+2/DIPol-2	0.87 ± 0.11	-0.50 ± 0.11	0.72 ± 0.10	-0.65 ± 0.10	0.93 ± 0.07	-0.39 ± 0.07
Ref 2/RoboPol	–	–	–	–	0.22 ± 0.21	-0.74 ± 0.14
Intrinsic polarization of Cyg X-1/HDE 226868						
	PD (%)	PA (deg)	PD (%)	PA (deg)	PD (%)	PA (deg)
Ref 2/DIPol-2	0.79 ± 0.17	-23 ± 6	0.83 ± 0.14	-26 ± 5	0.77 ± 0.15	-27 ± 6
Ref 1+2/DIPol-2	1.00 ± 0.11	-15 ± 3	0.97 ± 0.10	-21 ± 3	1.01 ± 0.07	-11 ± 2
Ref 2/RoboPol	–	–	–	–	0.77 ± 0.15	-37 ± 6

Table S4: Optical polarization of Cyg X-1/HDE 226868. Normalized Stokes parameters q and u are presented for the observed polarization of the source, the IS polarization, and the intrinsic polarization obtained by subtracting the IS polarization from the observed values. The polarization degree and polarization angle of the intrinsic polarization are computed using formulae (S2). Errors are 1σ .